Supplementary information for

Carbon-Embedded Mesoporous Nb-Doped TiO_2 Nanofibers as Catalyst Support for Oxidation Reduction Reaction in PEM Fuel Cells

Esmaeil Navaei Alvar, [a] Biao Zhou [a1] and S. Holger Eichhorn[b]

[a] Department of Mechanical, Automotive and Materials Engineering, University of Windsor, Windsor, Ontario, Canada.

[b] Department of Chemistry and Biochemistry, University of Windsor, Windsor, Ontario, Canada.

Table of Contents

[1]Principal Investigator and Corresponding Author: Biao Zhou (bzhou@uwindsor.ca).

Koutecky-Levich Equation [1, 2]

$$\frac{1}{j} = \frac{1}{j_k} + \frac{1}{B\omega^{1/2}} \qquad \text{(S-1)}$$

Where j is the experimentally measured current density ($mA.cm^{-2}$), j_k is kinetic current density ($mA.cm^{-2}$), j_d is the diffusion limiting current density ($mA.rad^{1/2}.s^{-1/2}.cm^{-2}$) and ω is the angular velocity frequency of rotation derived from $\omega=2\pi f/60$, f is the rotation rate in rpm. Constant B in Eq. (5) which is the simplified form of koutecky-Levich (K-L) equation by assuming the resistance of Nafion layer sufficiently small[3], can be expressed as follow:

$$B = 0.62nFD_{O_2}^{\frac{2}{3}} C_{O_2} \nu^{-\frac{1}{6}} \qquad \text{(S-2)}$$

The theoretical values for 2-electron (n=2) and 4-electron (n=4) ORR pathways can be calculated by extracting diffusion coefficient of O_2 ($D_{02} = 1.4 \times 10^{-5}$ $cm^2.s^{-1}$), maximum solubility of O_2 ($C_{O2} = 1.1 \times 10^{-6}$ $mol.cm^{-3}$), and kinematic viscosity of O_2 ($\nu = 10 \times 10^{-3}$ $cm^2.s^{-1}$) in 0.5 M H_2SO_4 aqueous solution at room temperature from literature.[4]

t-plots

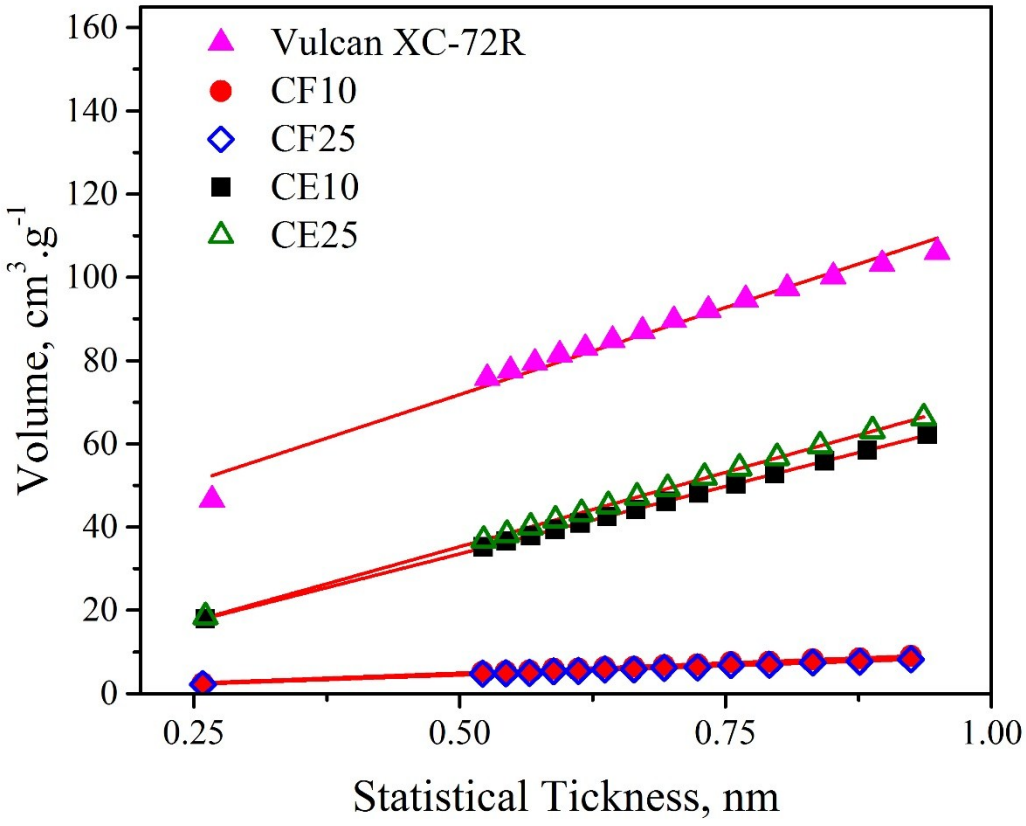

Figure S1. t-plots of all synthesized $Nb_xTi_{(1-x)}O_2$ (x = 0.1 and 0.25) nanofibers and a Vulcan XC-72R.

Raman peak analysis parameters and results

Table S1. Sadezky et al.[5] reported vibration modes and line shapes for the best curve-fitting of first-order Raman bands for carbonaceous materials.

Band	Raman Shift (cm^{-1})	Vibration mode	Line shape
G	~ 1580 cm^{-1}	Ideal graphitic lattice (E_{2g}-symmetry)	Lorentzian
D1	~ 1350 cm^{-1}	Disordered graphitic lattice (graphene layer edges, A_{1g} symmetry)	Lorentzian
D2	~ 1620 cm^{-1}	Disordered graphitic lattice (surface graphene layers, E_{2g} symmetry)	Lorentzian
D3	~ 1500 cm^{-1}	Amorphous carbon	Gaussian
D4	~ 1200 cm^{-1}	Disordered graphitic lattice (A_{1g} symmetry)	Lorentzain

Table S2. Relative band area ratios of the D1-D4 bands to G band, $A_{DX\text{-band}}/A_{G\text{-band}}$ (X = 1, 2, 3, 4).

Nanofiber Name	Peak Area Ratio			
	D1/G	D2/G	D3/G	D4/G
CE10	8.478	1.244	1.609	0.500
CE25	6.56	0.923	1.200	0.1212

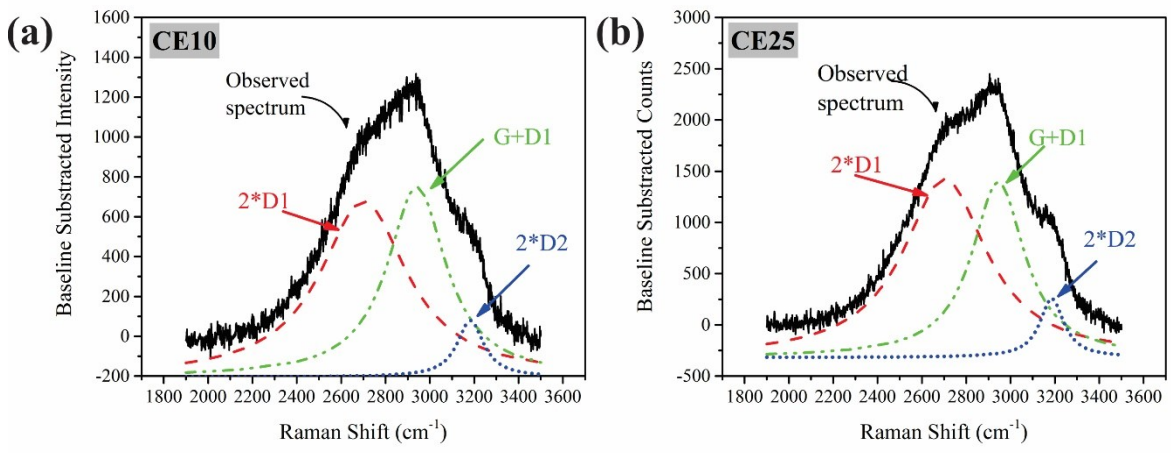

Figure S2. Peak analyses of the ordered/disordered graphite second-order bands observed in the Raman spectra of CE-NFs. (a) CE10; and (b) CE25.

PXRD patterns of Pt-deposited nanofibers

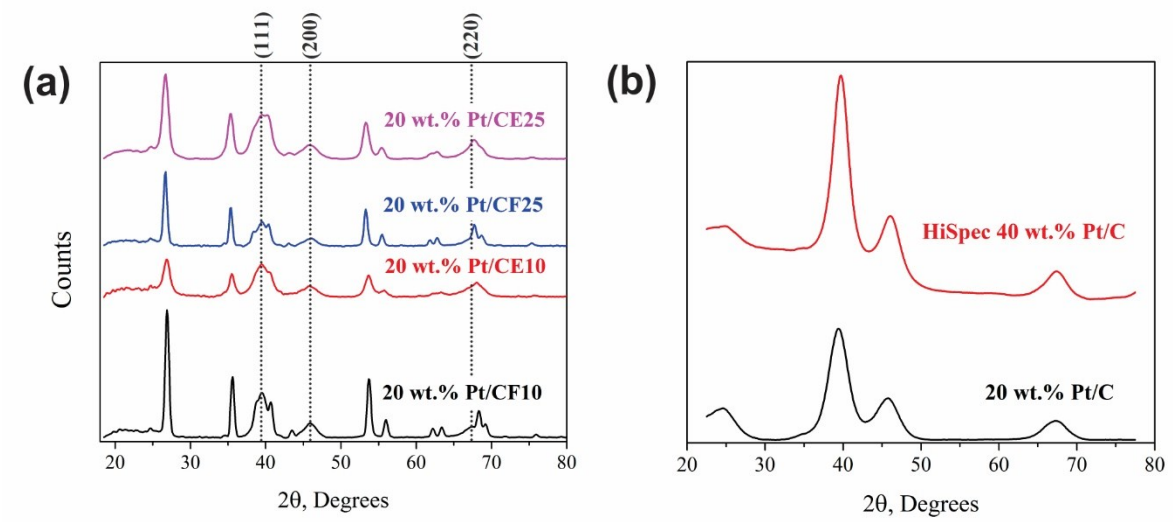

Figure S3. PXRD patterns of 20 wt. % Pt deposited $Nb_xTi_{(1-x)}O_2$ (x = 0.1 and 0.25) nanofibers.

Transmission electron microscopy (TEM) and energy dispersive X-ray spectroscopy (EDX) results

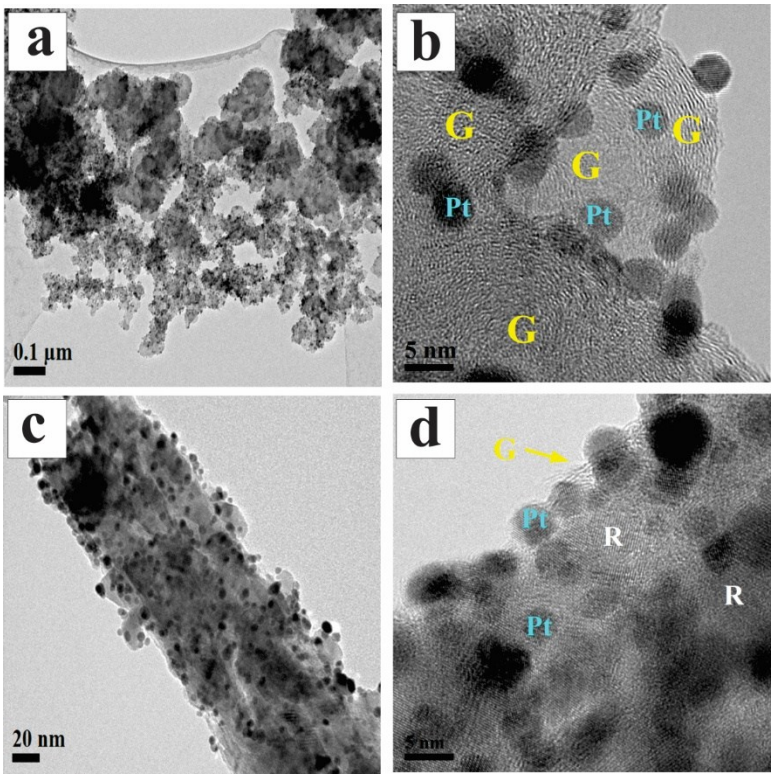

Figure S4. BF-TEM and HRTEM images from (a, b) 20 wt. % Pt/C and (c, d) 20 wt. % Pt/CE-25 samples.

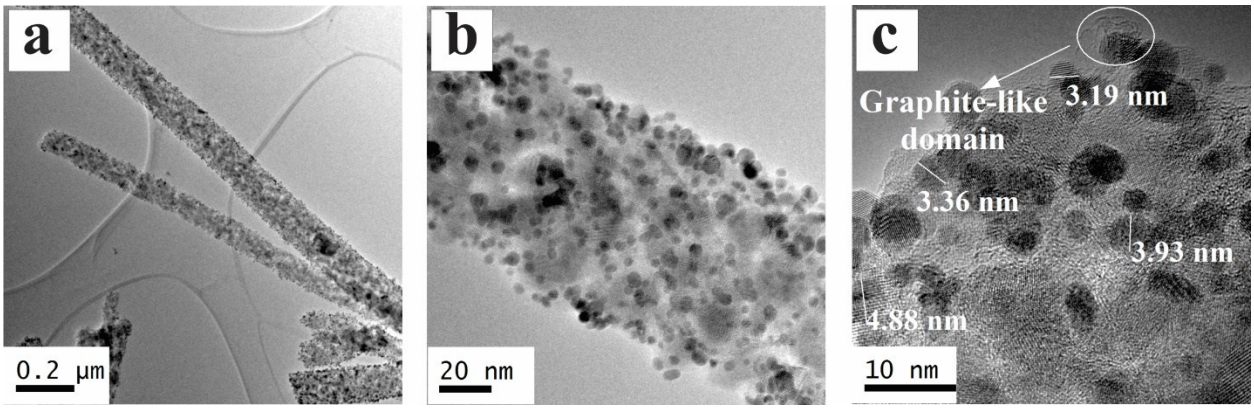

Figure S5. BF-TEM and HRTEM images of 20 wt. % Pt deposited CE10 nanofibers at different magnifications.

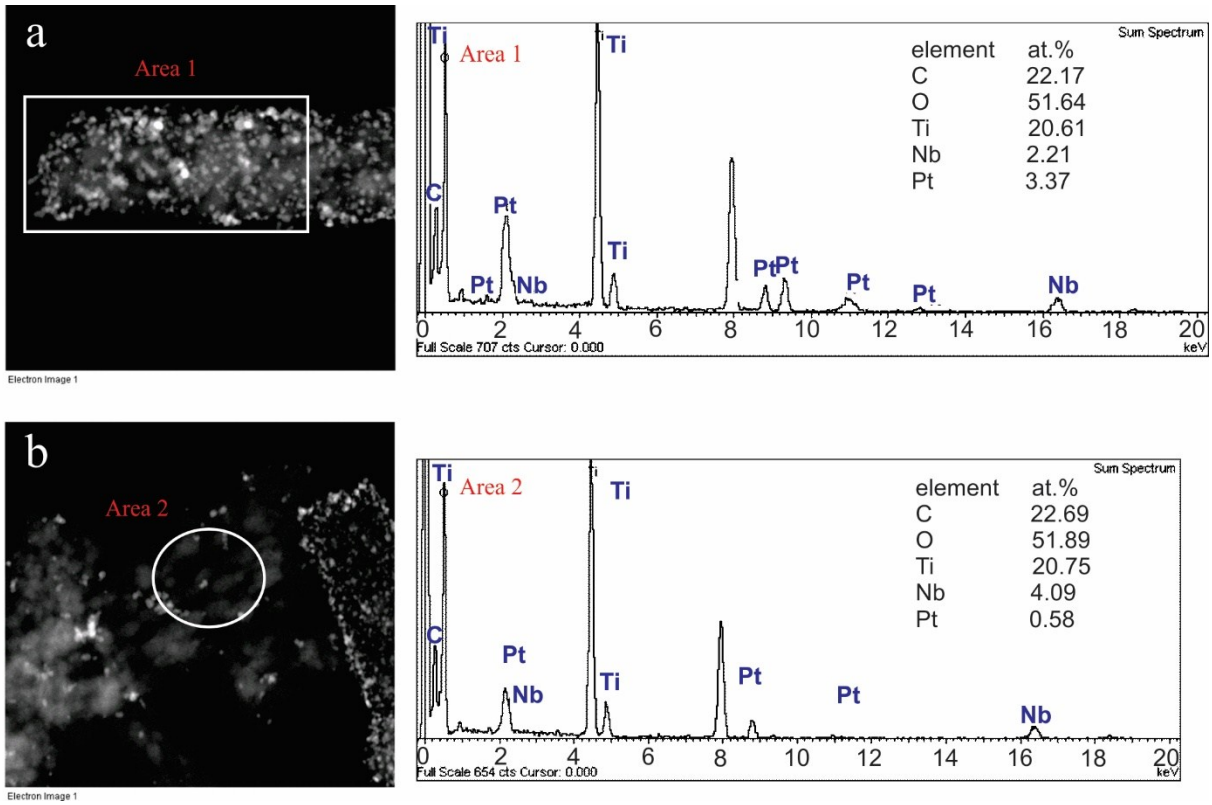

Figure S6. Dark field-TEM images and collected EDX spectra from 20 wt. % Pt deposited CE10 nanofibers.

X-ray photoelectron spectroscopy (XPS) survey scans

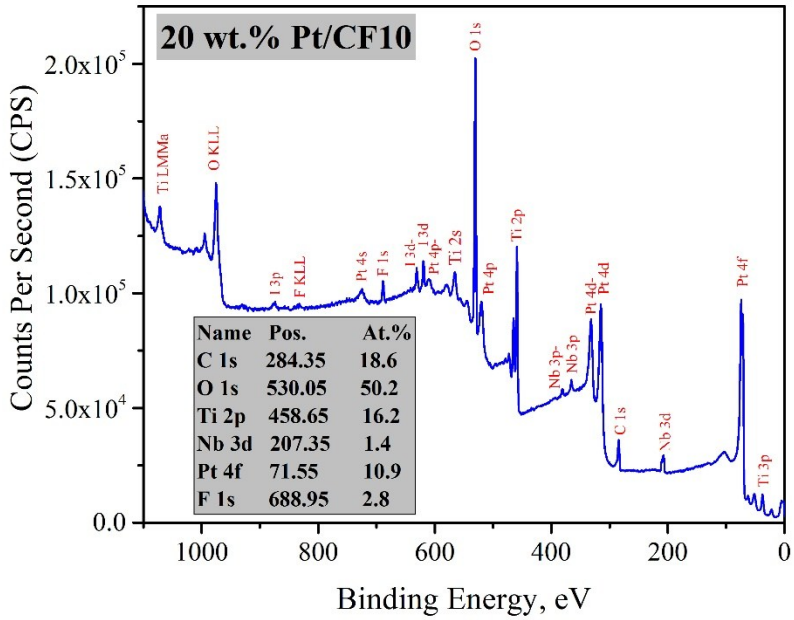

Figure S7. XPS survey spectra of 20 wt. % Pt deposited CF10 nanofibers.

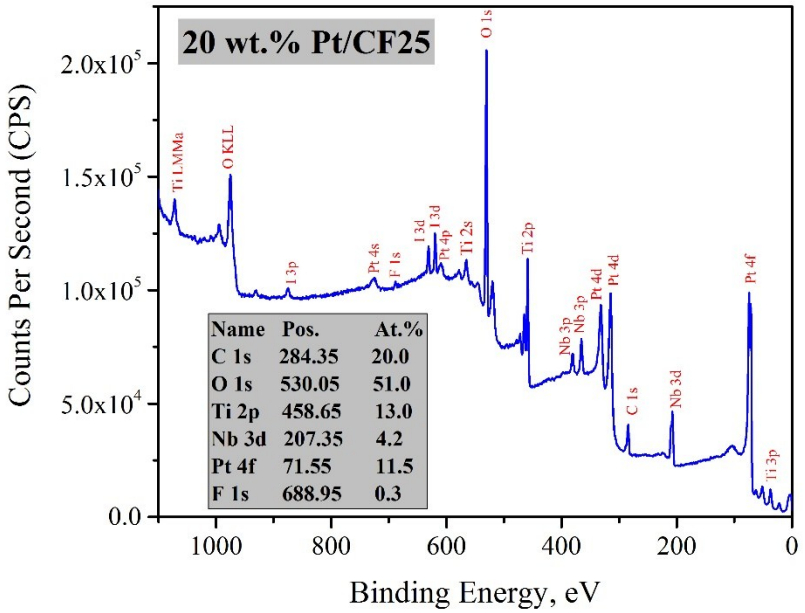

Figure S8. XPS survey spectra of 20 wt. % Pt deposited CF25 nanofibers.

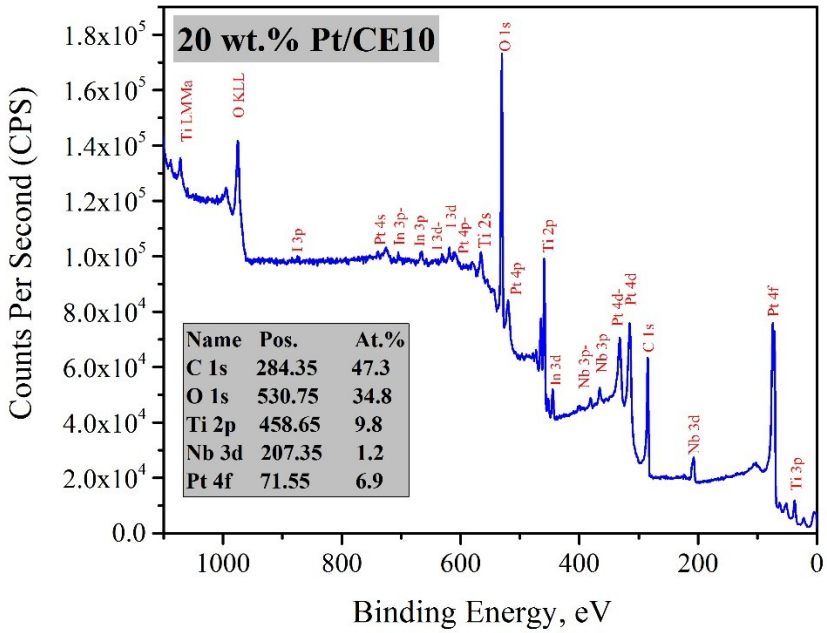

Figure S9. XPS survey spectra of 20 wt. % Pt deposited CE10 nanofibers.

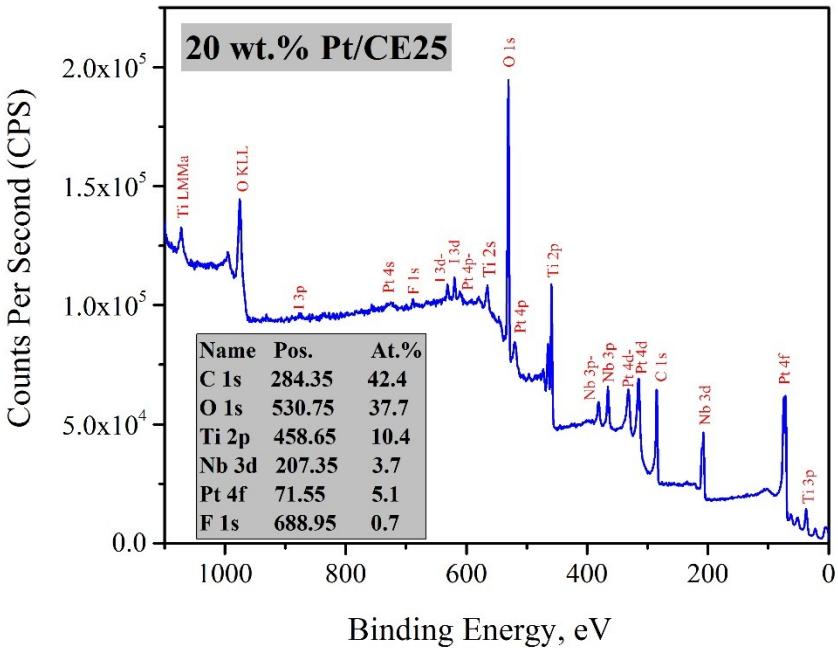

Figure S10. XPS survey spectra of 20 wt. % Pt deposited CE25 nanofibers.

High-resolution XPS scans in C 1s region

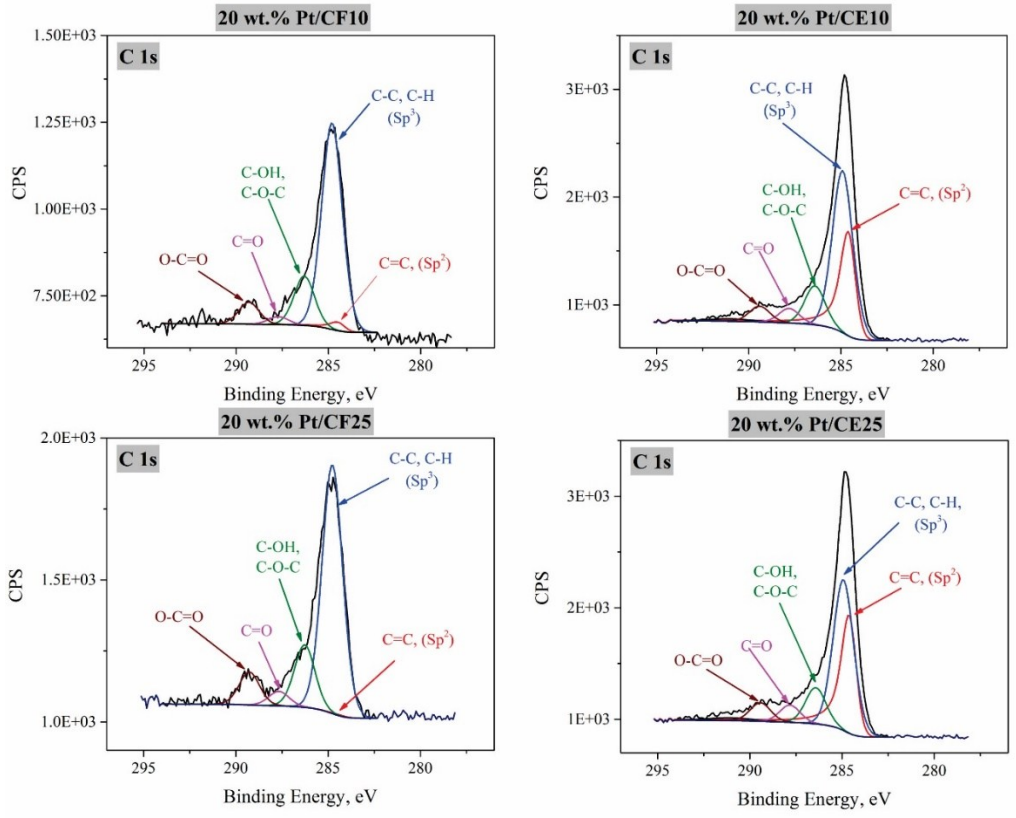

Figure S11. High resolution XPS spectra of different catalysts along with component fits in C 1s region.

Table S3. XPS peak parameters and Area % of different components in C 1s region.

Sample #	CF10				CE10				CF25				CE25			
At.% of C1s	18.6				47.3				20				42.4			
Chemical State	C=C, Sp^2	C-C, Sp^3	C-OH	Functional groups	C=C, Sp^2	C-C, Sp^3	C-OH	Functional groups	C=C, Sp^2	C-C, Sp^3	C-OH	Functional groups	C=C, Sp^2	C-C, Sp^3	C-OH	Functional groups
Peak Position, eV	284.51	28.81	286.31	287.71, 289.31	284.61	284.91	286.41	287.81, 289.41	284.47	284.77	286.27	287.67, 289.27	284.63	284.93	286.43	287.83, 289.43
FWHM	0.9	1.30	1.30	1.30	0.9	1.30	1.30	1.30	0.9	1.30	1.30	1.30	0.9	1.30	1.30	1.30
Area %	2	70.9	16.9	10.2	23.6	53.5	14.8	10	0.2	69.2	17.14	13.1	26.6	49.7	12	11.8
Sp^3/Sp^2	34.45				2.26				346				1.86			

High-resolution XPS scans in O 1s region

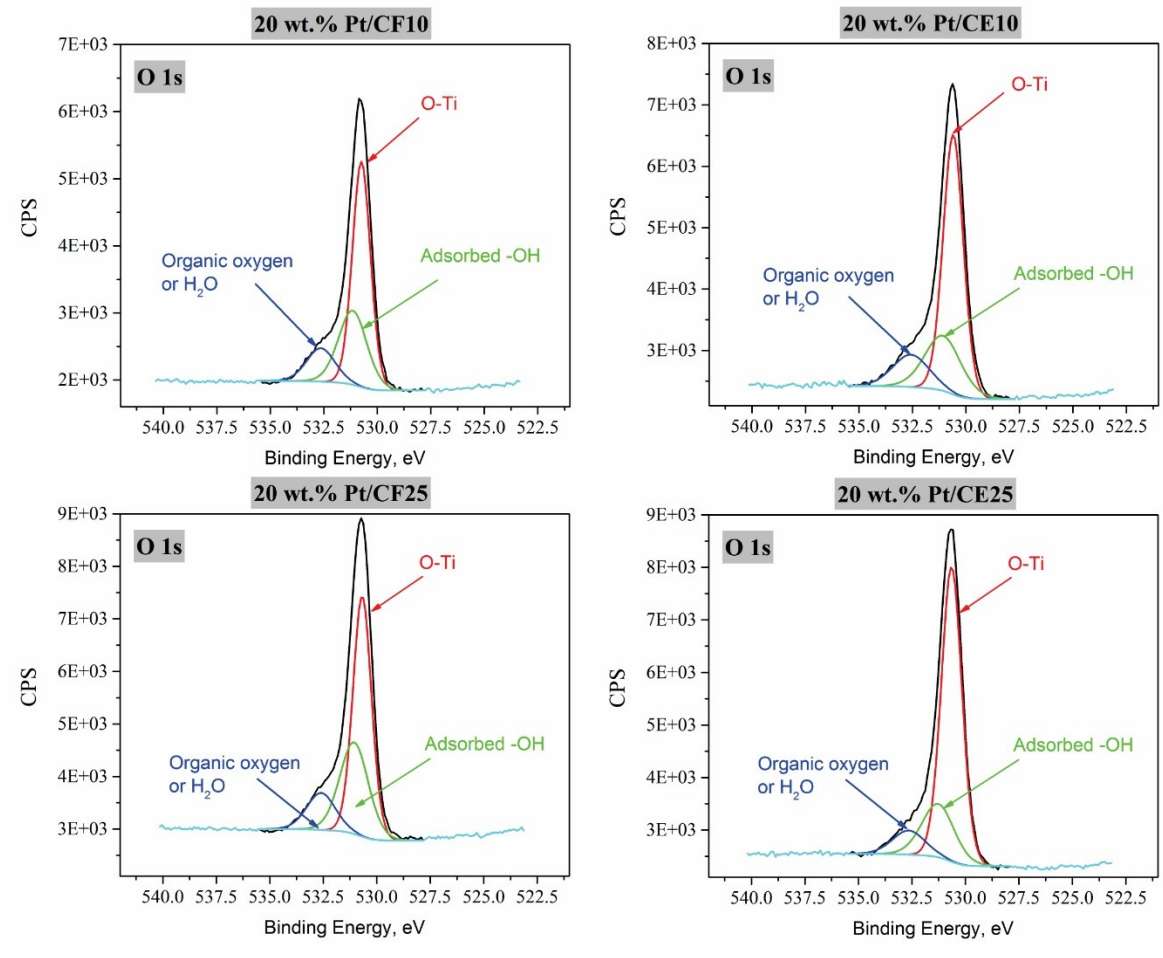

Figure S12. High resolution XPS spectra of different catalysts along with component fits in O 1s region.

Table S4. XPS peak parameters and Area % of different components in O 1s region.

Sample #	**CF10**			**CE10**			**CF25**			**CE25**		
At.% of O1s	50.2			34.8			51.0			37.7		
Chemical State	Oxide	Adsorbed -OH	Organic oxygen	Oxide	Adsorbed -OH	Organic oxygen	Oxide	Adsorbed -OH	Organic oxygen	Oxide	Adsorbed -OH	Organic oxygen
Peak Position, eV	530.74	531.14	532.64	530.59	531.07	532.57	530.68	531.05	532.60	530.64	531.27	532.65
FWHM	0.99	1.57	1.57	2	2	1.11	1.58	1.58	1.02	1.22	1.22	1.50
Area %	57.1	29.6	13.3	62.2	23.8	14.0	54.7	32.3	13.0	76	14.2	9.8

High-resolution XPS scans in Ti 2p region

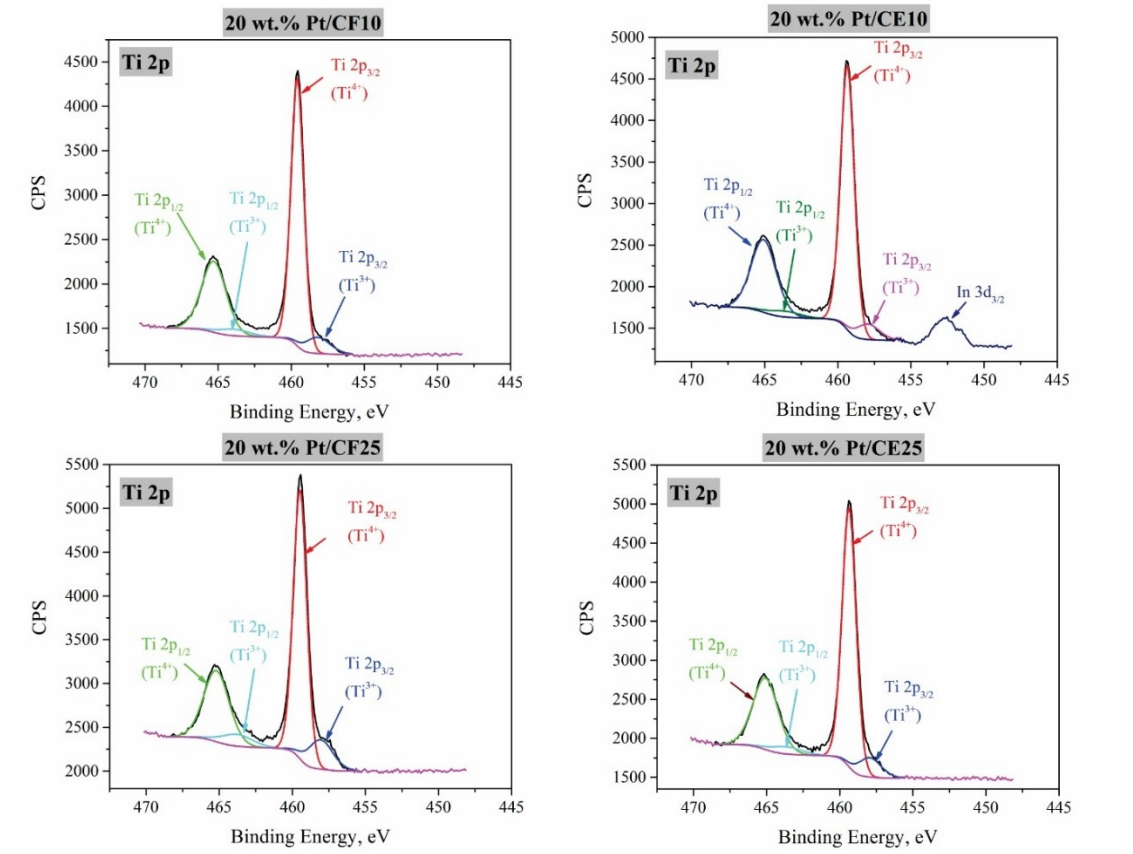

Figure S13. High resolution XPS spectra of different catalysts along with component fits in Ti 2p region.

Table S5. XPS peak parameters and Area % of different components in Ti 2p region.

Sample #	**CF10**		**CE10**		**CF25**		**CE25**	
At.% of Ti2p	16.2		9.8		13		10.4	
Chemical State	Ti $2p_{3/2}$ (Ti^{4+})	Ti $2p_{3/2}$ (Ti^{3+})	Ti $2p_{3/2}$ (Ti^{4+})	Ti $2p_{3/2}$ (Ti^{3+})	Ti $2p_{3/2}$ (Ti^{4+})	Ti $2p_{3/2}$ (Ti^{3+})	Ti $2p_{3/2}$ (Ti^{4+})	Ti $2p_{3/2}$ (Ti^{3+})
Peak Position, eV	459.59	463.91	459.35	457.95	459.47	458.07	459.36	457.96
FWHM	1.05	2.00	1.11	1.88	1.08	2.00	1.12	1.88
Area %	89.7	10.3	90.9	9.1	83.3	16.7	88.9	11.1

*Peak splitting value for Ti2p spin-orbit components is 5.72 eV.

High-resolution XPS scans in Nb 3d region

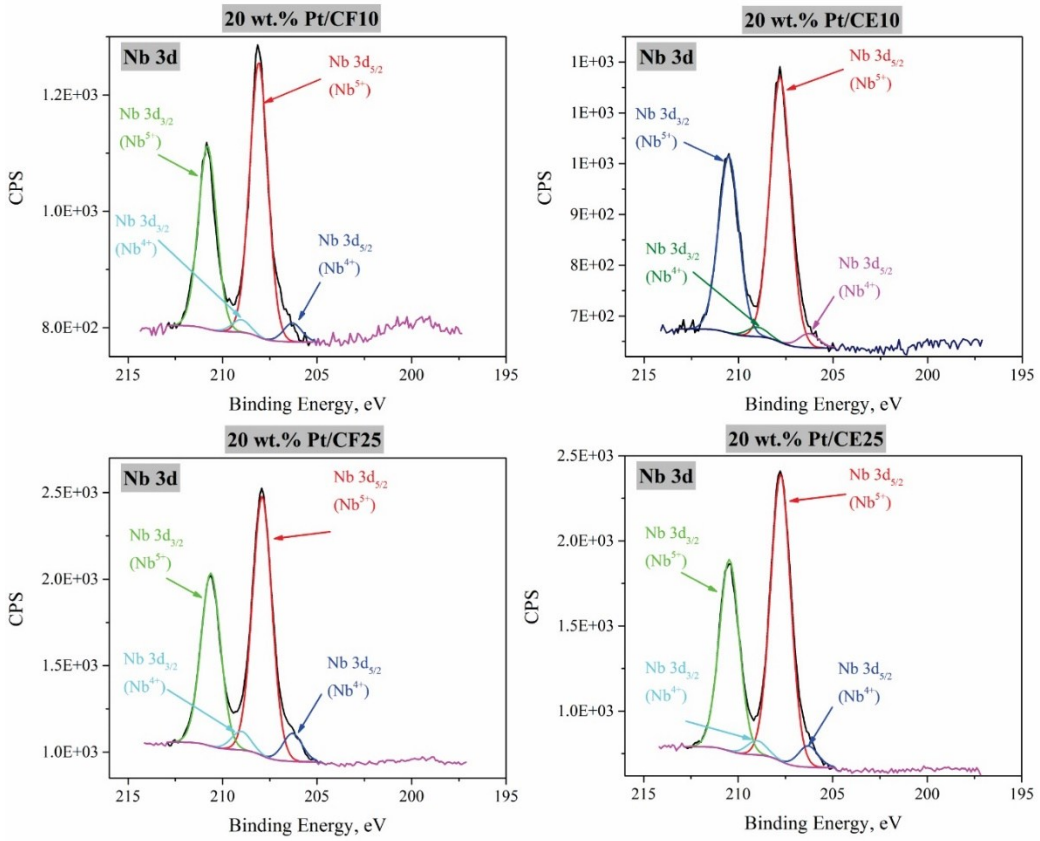

Figure S14. High resolution XPS spectra of different catalysts along with component fits in Nb 3d region.

Table S6. XPS peak parameters and Area % of different components in Nb 3d region.

Sample #	**CF10**		**CE10**		**CF25**		**CE25**	
At.% of Nb3d	1.4		1.2		4.2		3.7	
Chemical state	Nb $3d_{5/2}$ (Nb^{5+})	Nb $3d_{5/2}$ (Nb^{4+})	Nb $3d_{5/2}$ (Nb^{5+})	Nb $3d_{5/2}$ (Nb^{4+})	Nb $3d_{5/2}$ (Nb^{5+})	Nb $3d_{5/2}$ (Nb^{4+})	Nb $3d_{5/2}$ (Nb^{5+})	Nb $3d_{5/2}$ (Nb^{4+})
Peak Position, eV	208.08	206.30	207.80	206.30	207.91	206.30	207.75	206.30
FWHM	1.13	1.13	1.26	1.26	1.21	1.21	1.24	1.24
Area %	93.6	6.4	94.9	5.1	90.2	9.8	93.1	6.9

*Peak splitting value for Nb3d spin-orbit components is 2.72 eV.

High-resolution XPS scans in Pt 4f region

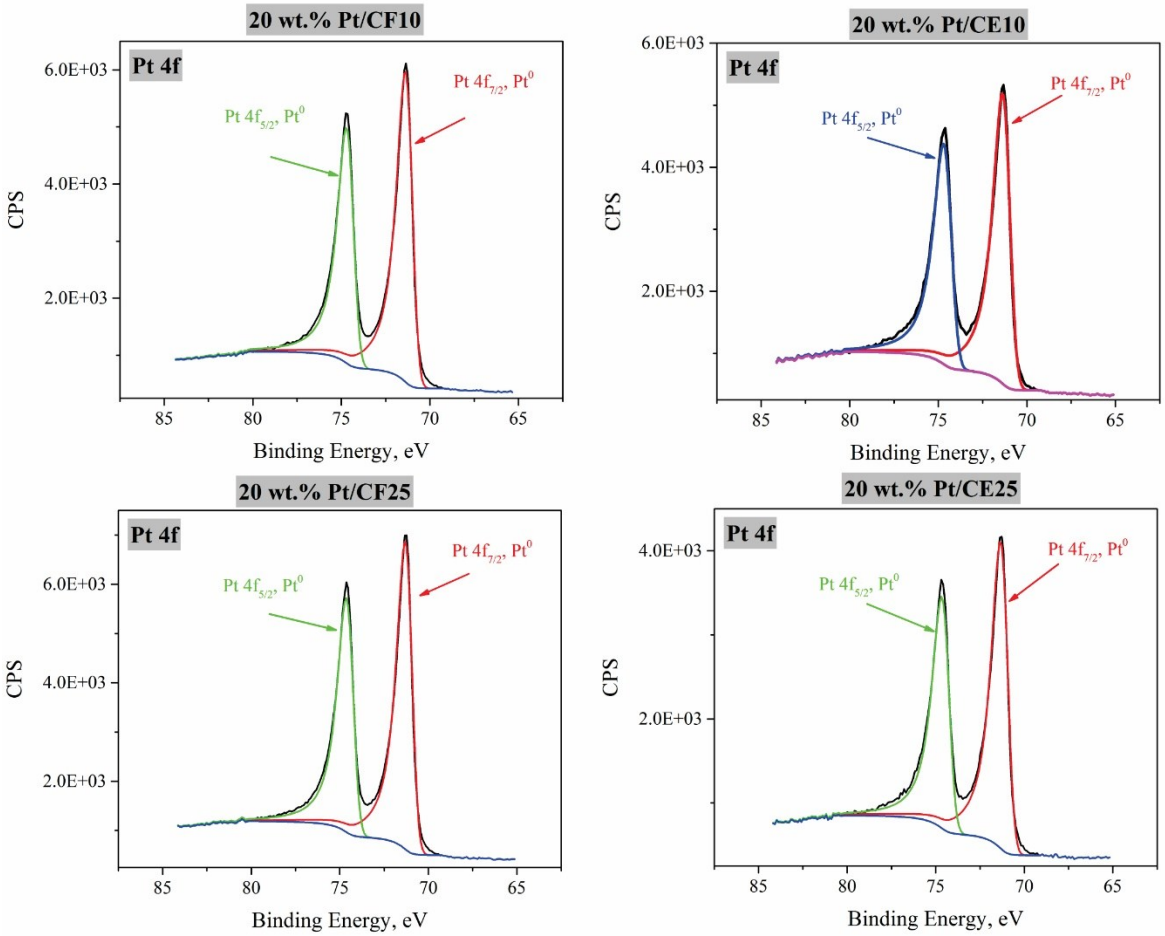

Figure S15. High resolution XPS spectra of different catalysts along with component fits in Pt 4f region.

Table S7. XPS peak parameters and Area % of different components in Pt 4f region.

Sample #	**CF10**	**CE10**	**CF25**	**CE25**
At.% of Pt4f	10.9	6.9	11.5	5.1
Chemical state	Pt $4f_{7/2}$ (Pt^0)	Pt $4f_{7/2}$ (Pt^0)	Pt $4f_{7/2}$ (Pt^0)	Pt $4f_{7/2}$ (Pt^0)
Peak Position, eV	71.10	71.07	71.03	71.05
FWHM	0.90	0.96	0.88	0.93

*Peak splitting value for Pt4f spin-orbit components is 3.32 eV.

Kroger-vink notations

$$\frac{1}{2}Nb_2O_5 + Ti_{Ti}^{\times} \rightarrow Nb_{Ti}^{\circ} + \frac{1}{4}V_{Ti}^{''''} + TiO_2 + \frac{1}{2}O_2 \qquad \text{(S-3)}$$

$$\frac{1}{2}Nb_2O_5 + Ti_{Ti}^{\times} \rightarrow Nb_{Ti}^{\circ} + Ti_{Ti}^{'} + \frac{5}{2}O_2 \qquad \text{(S-4)}$$

Table S8. Descriptions of Kroger-vink notations used in Eqs. (3) and (4).

Kroger-vink notation	Description	
Ti_{Ti}^{X}	A titanium ion siting on a titanium lattice site with neutral charge	(Ti^{4+})
Nb_{Ti}°	A niobium ion sitting on a titanium lattice site with single positive charge	(Nb^{5+})
$V_{Ti}^{''''}$	A titanium vacancy with quadruple negative charge	
$Ti_{Ti}^{'}$	A titanium ion siting on a titanium lattice site with single negative charge	(Ti^{3+})

Electrochemical characterization results

Table S9. Changes on Pt oxide reduction onset potential and oxygen reduction reaction half-potential of the synthesized and commercial catalysts.

Catalyst	Before Durability Tests		After Durability Tests	
	Pt Oxide Reduction Onset Potential (V)	ORR $E_{1/2}$ (V)	Change in Onset Potential (mV)	ORR $E_{1/2}$ (V)
20 wt.% Pt/CF10	0.812	0.783	10	0.768
20 wt.% Pt/CF25	0.812	0.687	10	0.670
20 wt.% Pt/CE10	1.13	0.835	3	0.825
20 wt.% Pt/CE25	1.10	0.828	3	0.815
20 wt.%Pt/C	1.16	0.836	0	0.812
HiSpec 40 wt.% Pt/C	1.15	0.837	0	0.808

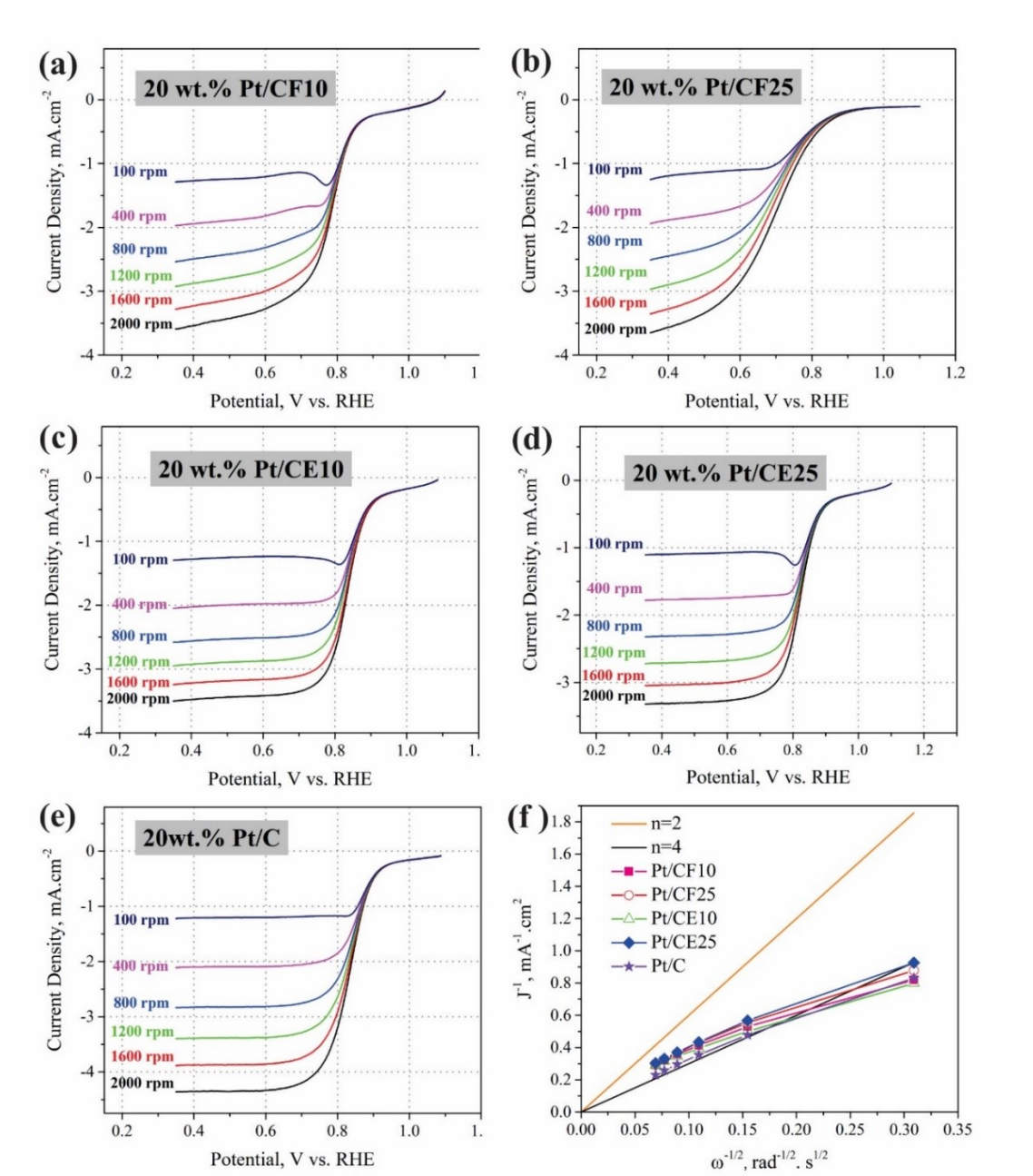

Figure S16. ORR Linear sweep voltammograms (LSVs) recorded at a potential scan rate of 5 mV s^{-1} and various rotation speeds along with Koutecky-Levich plots at 0.7 V for different catalysts in O_2 saturated aqueous solution of 0.5M H_2SO_4. LSVs for (a) 20 wt.%Pt/CF10; (b) 20 wt.%Pt/CF25; (c) 20 wt.%Pt/CE10; (d) 20 wt.%Pt/CE25; (e) 20 wt.%Pt/Vulcan; and (f) K-L plots at 0.7V.

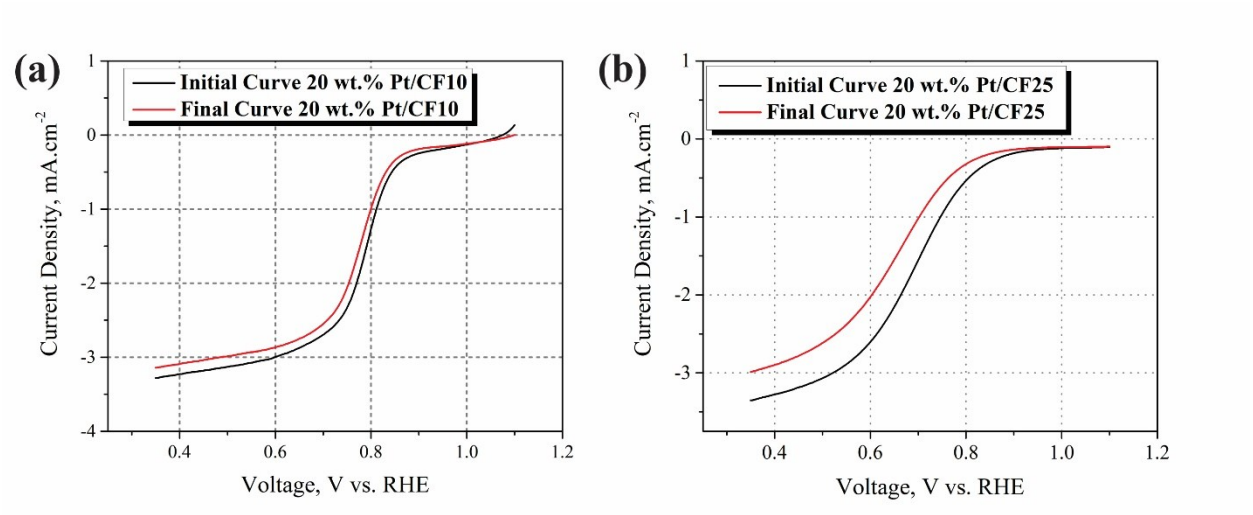

Figure S17. ORR linear sweep voltammograms of different catalysts recorded in O_2 saturated aqueous solutions of 0.5M H_2SO_4 with a potential sweep rate and rotation speed of 5 mV/s and 1600 rpm, respectively, before and after 1000 potential cycles. (a) 20 wt.% Pt/CF10; (b) 20 wt.% Pt/CF25.

References

1. K. Senevirathne, V. Neburchilov, V. Alzate, R. Baker, R. Neagu, J. Zhang, S. Campbell and S. Ye, Journal of Power Sources, 2012, 220, 1-9.
2. V. G. Levich, Physicochemical hydrodynamics, Prentice-Hall, Englewood Cliffs, N.J., 1962.
3. U. A. Paulus, A. Wokaun, G. G. Scherer, T. J. Schmidt, V. Stamenkovic, N. M. Markovic and P. N. Ross, Electrochimica Acta, 2002, 47, 3787-3798.
4. C. Song and J. Zhang, in PEM Fuel Cell Electrocatalysts and Catalyst Layers, ed. J. Zhang, Springer London, 2008, DOI: 10.1007/978-1-84800-936-3_2, ch. 2, pp. 89-134.
5. A. Sadezky, H. Muckenhuber, H. Grothe, R. Niessner and U. Pöschl, Carbon, 2005, 43, 1731-1742.